Supporting Information

Solution-Free Synthesis of MXene Composite Hybrid Nanostructures by Rapid Joule Heating

Jeesoo Yoon[§, ¶, ||], *Yong-Jae Kim*[§, ¶, ||], *Ji-Yoon Song*[§, ¶, ||], *Aqil Jamal*[δ], *Issam Gereige*[δ], *Chansol Kim**[, β], *Hee-Tae Jung**[, §, ¶, ||]

§Department of Chemical and Biomolecular Engineering (BK21 four), Korea Advanced Institute of Science and Technology (KAIST), 291 Daehak-ro, Yuseong-gu, Daejeon, Republic of Korea

¶KAIST-UC Berkeley-Vietnam National University Climate Change Research Center, KAIST, Daejeon 305-701, South Korea

|| Saudi Aramco-KAIST CO_2 management Center, KAIST, Daejeon 305-701, South Korea

βClean Energy Research Center, Korea Institute of Science and Technology (KIST), Seoul 02792, Republic of Korea

δSaudi Aramco, Research and Development Center, Dhahran, 31311, Saudi Arabia

E-mail: chansolkim@kist.re.kr; heetae@kaist.ac.kr

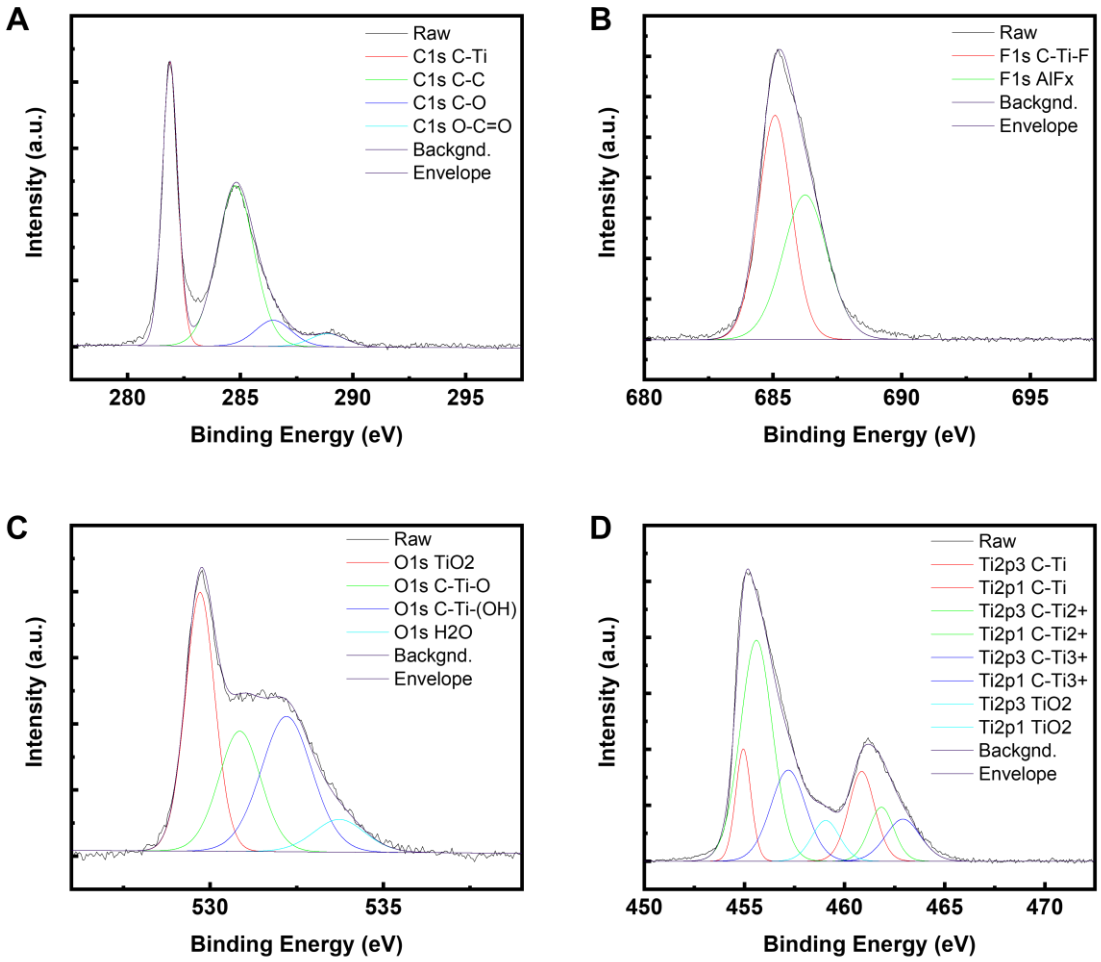

Fig. S1. XPS peaks of bare MXene. A) C1s peak. B) F1s peak. C) O1s peak. D) Ti2p peak.

$Ti_3C_2T_x$ MXene was successfully synthesized by the chemical wet-etching method. The synthesized $Ti_3C_2T_x$ MXene shows well-maintained abundant surface termination groups, including oxygen, fluorides and hydroxides

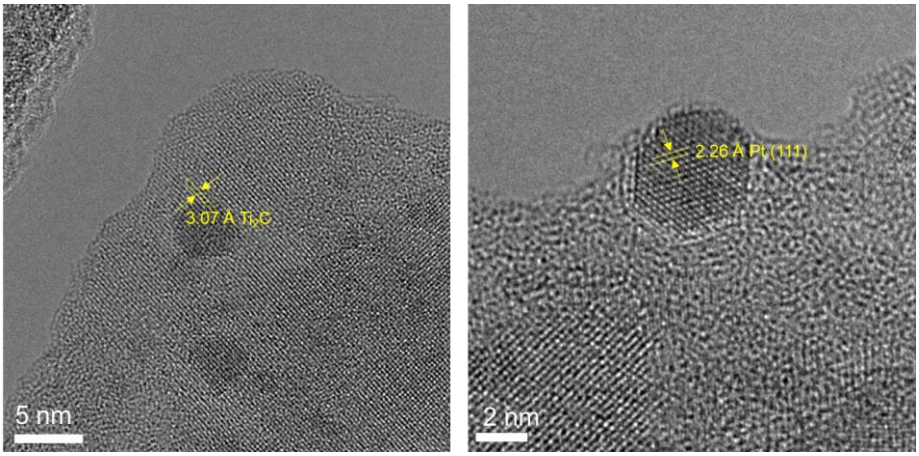

Fig. S2. HRTEM of Pt nanoparticles (NPs) on Ti_2CT_x MXene.

Rapid Joule heating method is also applicable to other types of MXenes. Pt NPs were well synthesized on Ti_2CT_x MXene substrate as confirmed by HRTEM analysis.

Fig. S3. MXene aerogel synthesis.

Synthesized MXene was fabricated into suitable morphology for rapid Joule heating. The MXene aerogel was synthesized by freeze-casting the MXene solution (10 mg/mL) for 24 hours at -80°C and freeze-drying for 72 hours at -110°C.

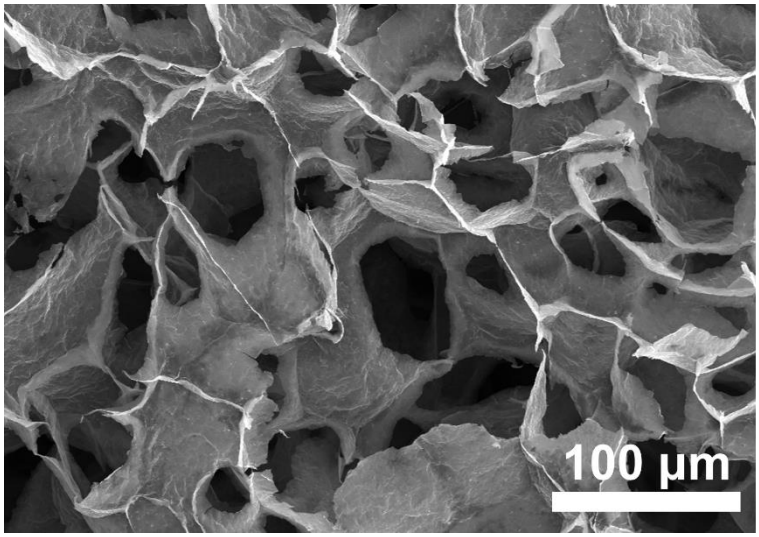

Fig. S4. MXene aerogel structure.

The synthesized MXene aerogel shows high surface area with abundant pores in its structure. The pore size ranged from 20 µm to 100 µm.

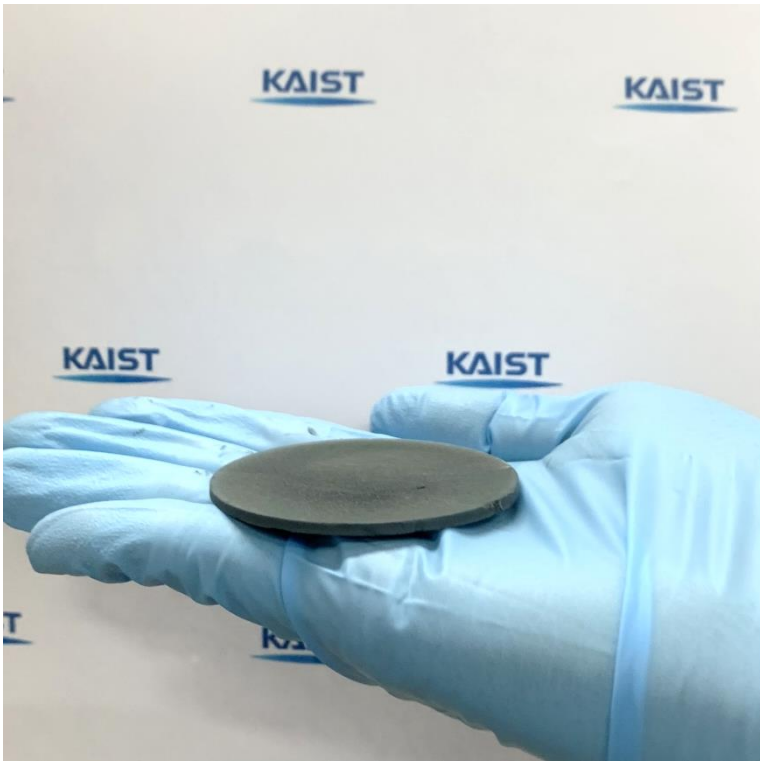

Fig. S5. Freestanding MXene aerogel.

The synthesized MXene aerogel is freestanding, which allows direct use as rapid Joule heating substrate without additional supporting material.

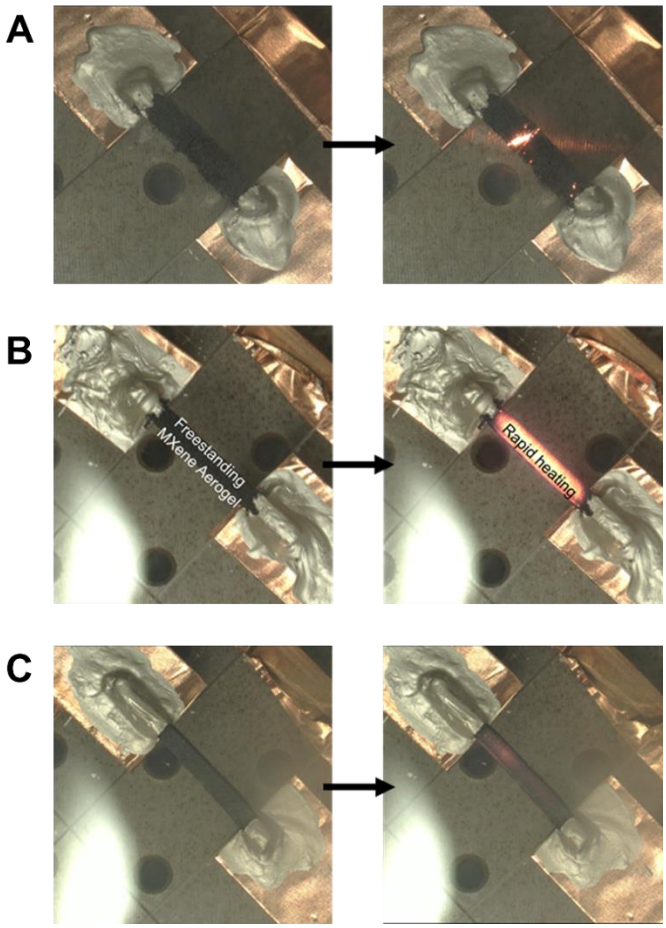

Fig. S6. Photo images of rapid heating process depending on concentration of MXene aerogel. A) Concentration of 5 mg/mL. B) Concentration of 10 mg/mL. C) Concentration of 15 mg/mL.

To undergo rapid Joule heating, the substrate should have sufficient mechanical strength to endure the heating process and appropriate resistance to irradiate heat. MXene aerogel synthesized from a low MXene solution concentration in **Fig. S6A** was too brittle that a spark was created when given the shock. On the other hand, MXene aerogel with high MXene solution concentration in **Fig. S6C** did not have enough resistance to undergo Joule heating upon thermal shock, thus showing dim light. With optimization of MXene solution concentration as in **Fig. S6B**, the aerogel emitted bright light under thermal shock.

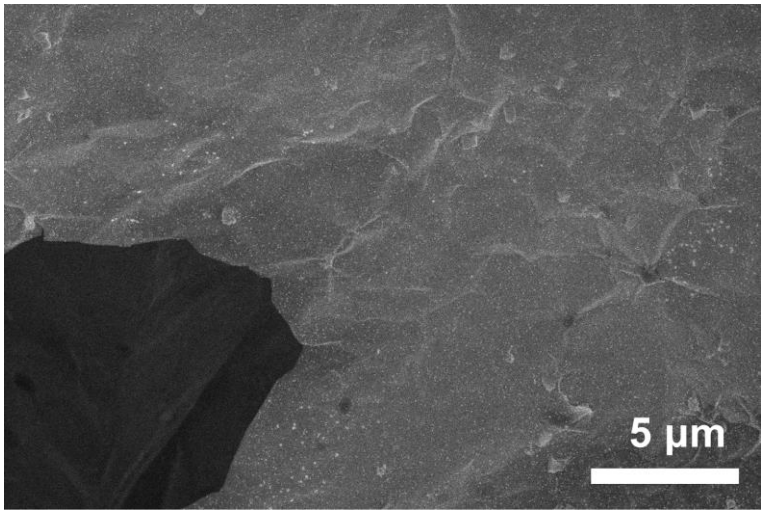

Fig. S7. SEM image of rapid heating Pt-MXene surface after rapid Joule heating.

After rapid Joule heating synthesis, Pt metal NPs were well synthesized over a large area, uniformly distributed on MXene surface.

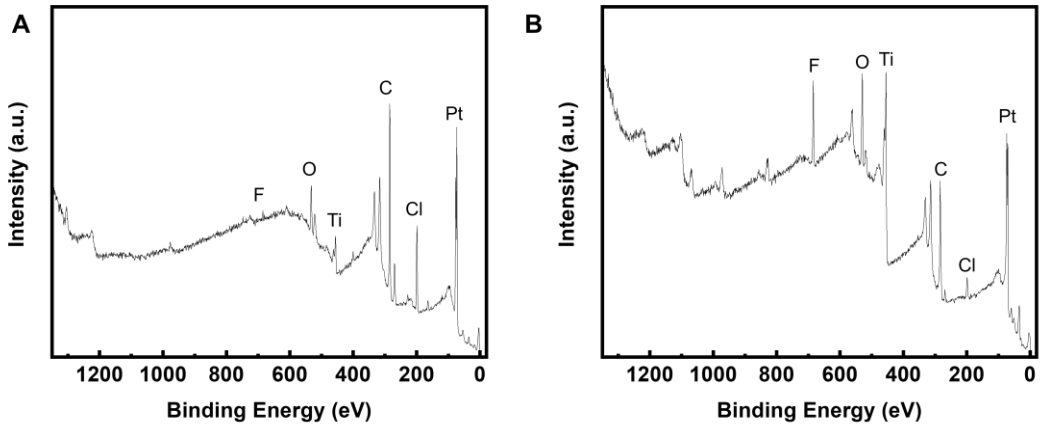

Fig. S8. XPS survey peaks of rapid heating Pt-MXene A) before rapid heating and B) after rapid heating.

After rapid heating process, the chloride peak in **Fig. S8A** from the liquid metal precursor was mostly evaporated as can be checked by the decreased Cl intensity in **Fig. S8B.**

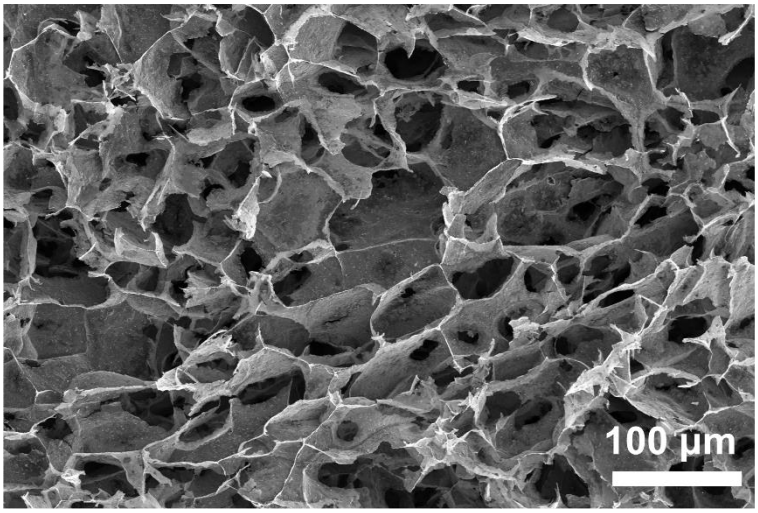

Fig. S9. MXene aerogel structure after rapid heating.

The MXene aerogel retained its structure even after rapid heating, indicating the non-destructive nature of this process.

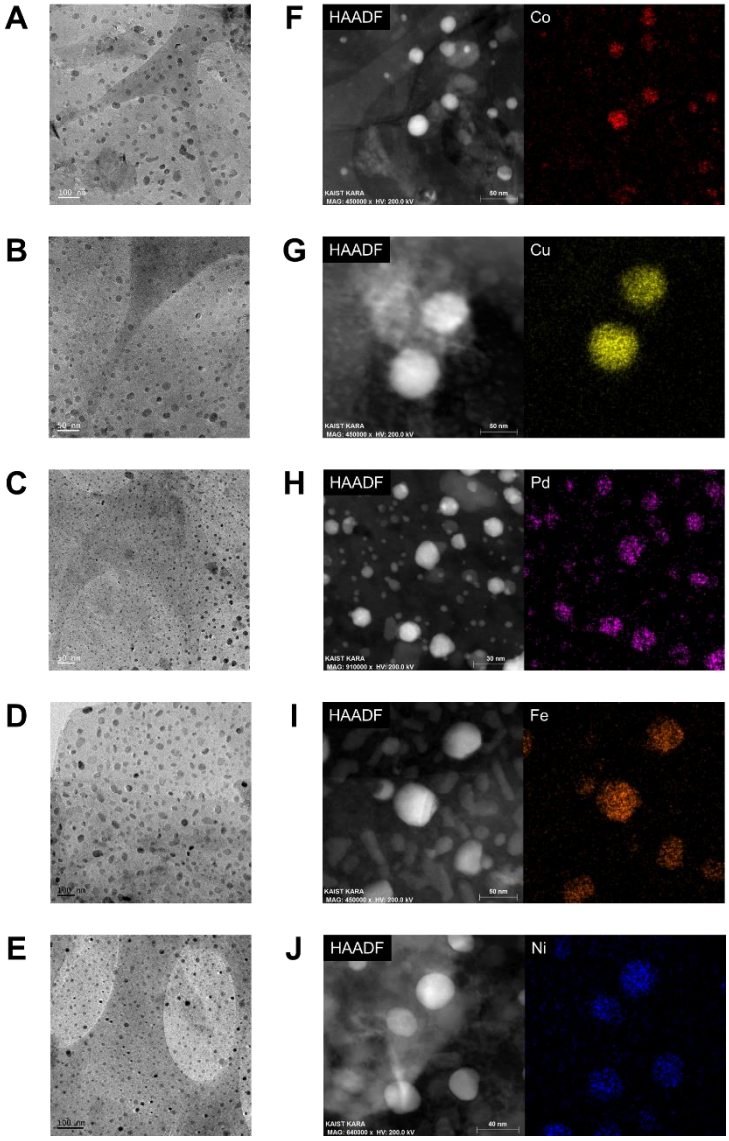

Fig. S10. Synthesis of single metal NPs on MXene surface. TEM images single metal NPs A) Co, B) Cu, C) Pd, D) Fe, E) Ni and STEM elemental maps of single metal NPs F) Co, G) Cu, H) Pd, I) Fe, J) Ni.

By simply changing the precursor type, various MXene composite hybrid nanomaterials can be fabricated. Single metal elements including Co, Cu, Pd, Fe, and Ni was prepared on MXene substrate.

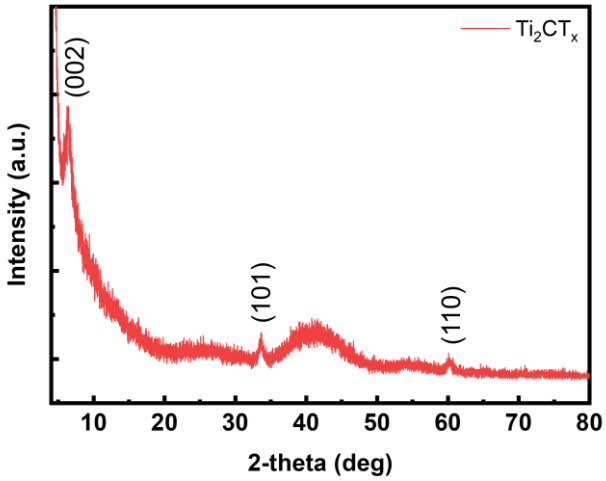

Fig. S11. XRD pattern of Ti_2CT_x MXene.

Ti_2CT_x MXene was prepared to show the universality of the rapid heating method. Ti_2AlC MAX phase was chemically wet etched for the preparation of Ti_2CT_x MXene. The synthesized product show characteristic XRD peaks corresponding to Ti_2CT_x MXene.

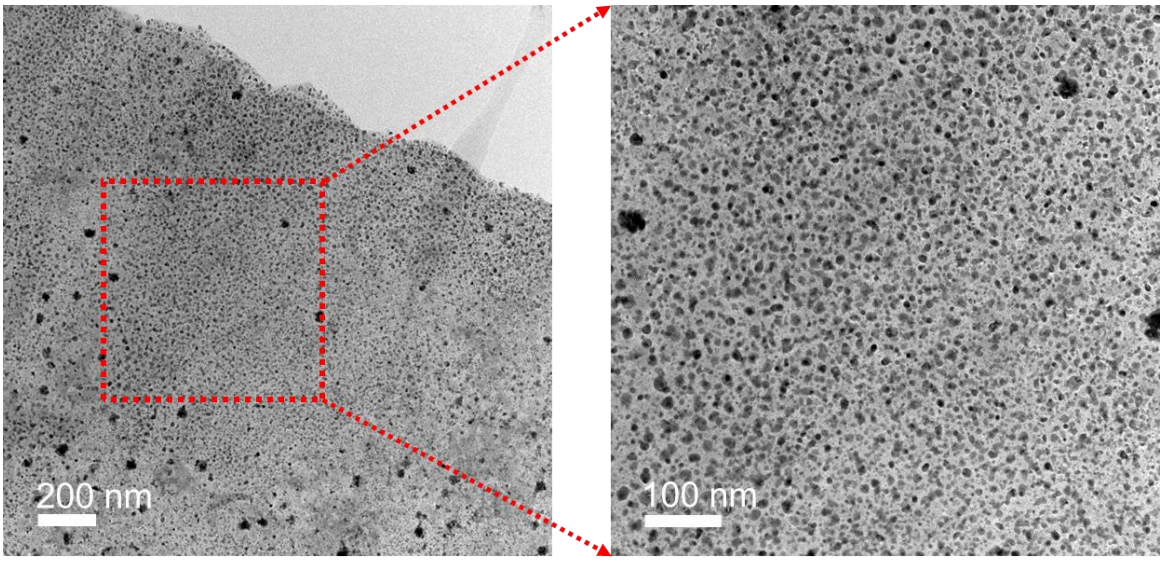

Fig. S12. TEM image of uniformly distributed Pt NPs on Ti_2CT_x MXene.

Pt NPs were uniformly synthesized on Ti_2CT_x MXene surface over a large area. The dense formation of NPs is attributed to the high density of oxygen termination in Ti_2CT_x MXene.

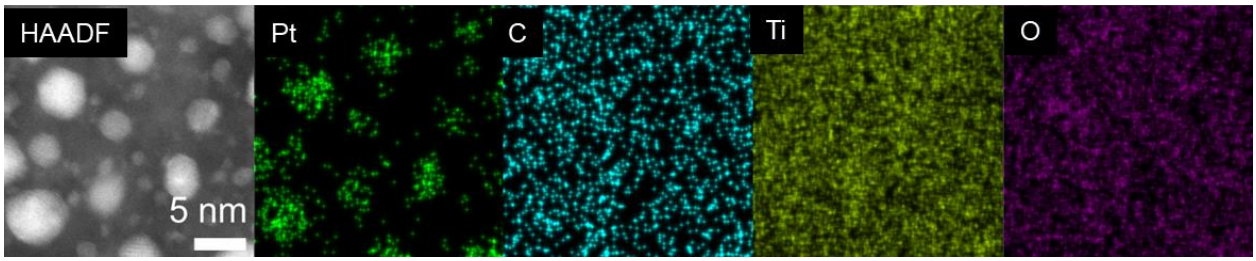

Fig. S13. STEM elemental maps of Pt NPs on Ti_2CT_x MXene surface.

Pt NPs synthesized on Ti_2CT_x MXene was further analyzed. Elements C, Ti, and O corresponding to the elements found in MXene substrate were also detected. The even distribution of these elements confirms that Ti_2CT_x MXene is preserved and that the formation of TiO_2 is effectively suppressed.

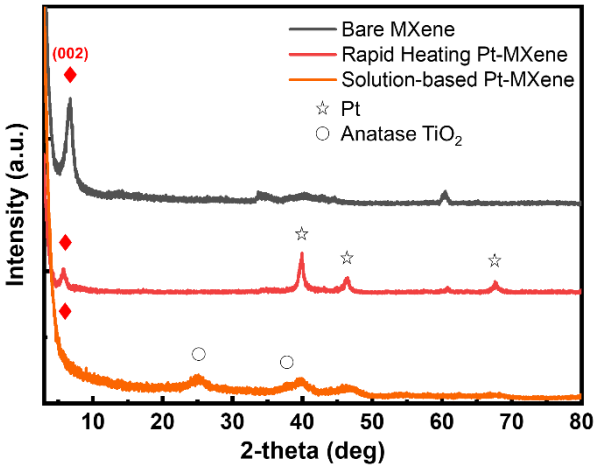

Fig. S14. XRD patterns of bare MXene, rapid heating Pt-MXene and solution-based Pt-MXene.

XRD patterns confirm the lower degree of MXene oxidation during MXene hybrid composite nanostructure synthesis using rapid heating. Rapid heating Pt-MXene showed characteristic peak of MXene after synthesis. The XRD pattern of solution-based Pt-MXene showed low intensity of the characteristic peak. Rather, it exhibited peaks of anatase-TiO_2, indicating high degree of MXene oxidation during synthesis

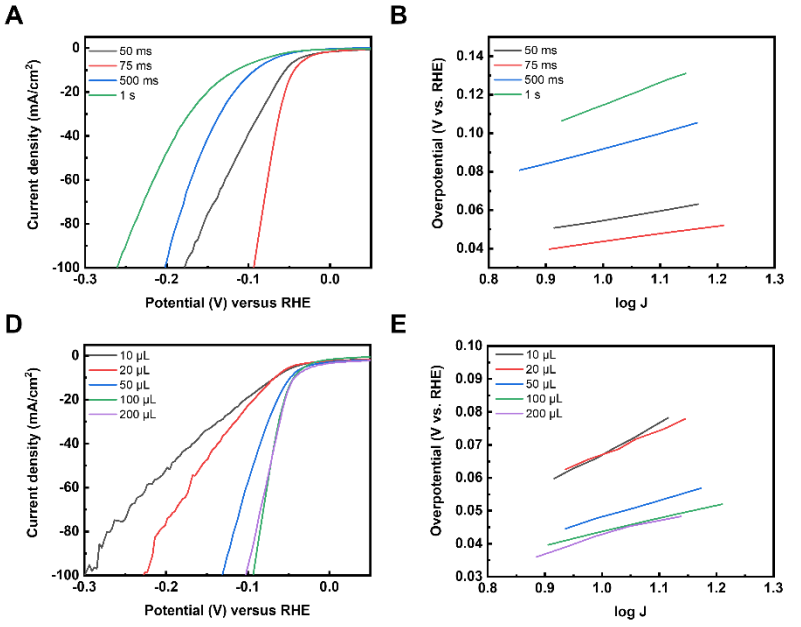

	Overpotential at 10mA/cm² (mV)	Tafel Slope (mV/dec)
Varying Rapid Heating Duration (100 µL loading)		
50 ms	54.5	49.1
75 ms	43.6	40.5
500 ms	91.7	79.4
1 s	114.6	114.9

	Overpotential at 10mA/cm² (mV)	Tafel Slope (mV/dec)
Varying Precursor Loading (75ms)		
10 µL	67	92.1
20 µL	66.9	72.6
50 µL	48.2	51.4
100 µL	43.6	40.5
200 µL	43.8	49.2

Fig. S15. Optimization of rapid heating Pt-MXene HER performance by varying rapid heating duration and precursor loading. A) Polarization curves, B) Tafel slopes, and C) overpotential values and Tafel slopes organized for varied rapid heating durations. D) Polarization curves, E) Tafel slopes, and F) overpotential values and Tafel slopes organized for varied precursor loadings.

When the rapid heating duration was increased, there was a general trend of decreasing HER performance which can be attributed to the increased MXene damage with increase in exposure to high temperature. Yet, when the duration of heating was insufficient (50 ms), Pt NPs were incompletely formed thus showing low performance.

With increase in precursor loading, the HER performance was overall increased. However, when the loading was excessive we did not observe a greater increase in the performance.

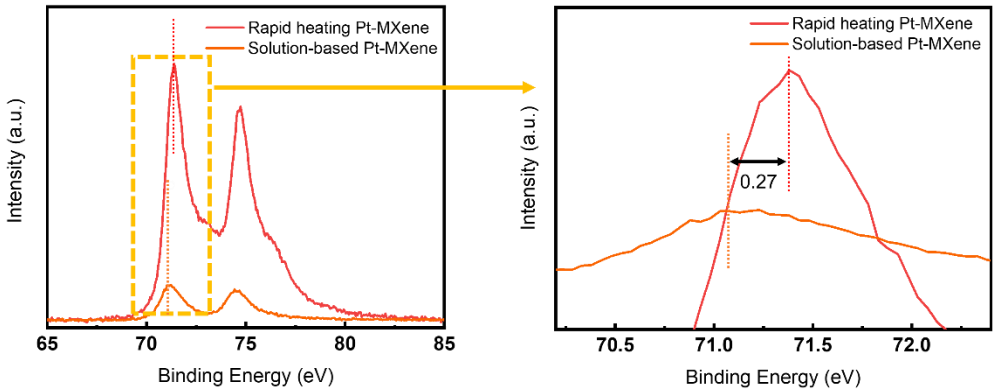

Fig. S16. XPS spectra of Pt4f on rapid heating Pt-MXene and solution-based processing Pt-MXene.

The rapid heating Pt-MXene demonstrated a higher binding energy position of Pt4f7/2 compared to solution-based processing Pt-MXene.

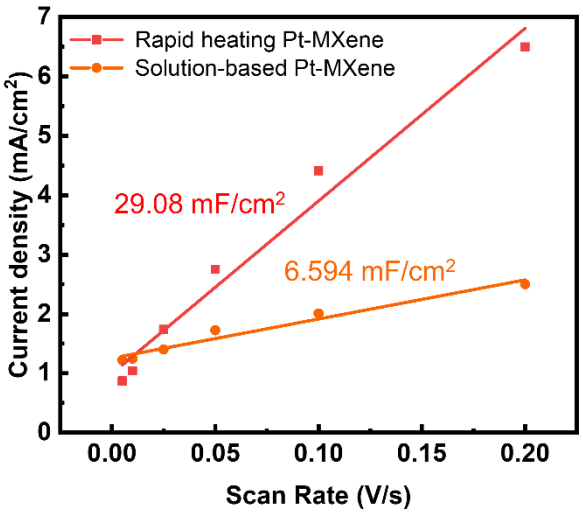

Fig. S17. Double layer capacitance of rapid heating Pt-MXene and solution-based Pt-MXene.

The double-layer capacitance (C_{dl}) was calculated to demonstrate the difference in electrochemically active surface area (ECSA) of the two catalysts. The higher C_{dl} of rapid heating Pt-MXene indicates larger ECSA and greater capacity for effective charge accumulation.

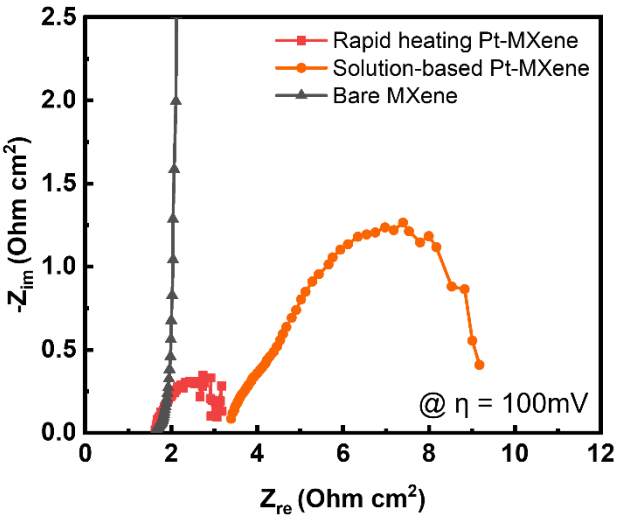

Fig. S18. Nyquist plot of rapid heating Pt-MXene and solution-based Pt-MXene.

The Nyquist plot was compared to examine the charge transfer resistance (R_{ct}) of the catalysts. The R_{ct} of rapid heating Pt-MXene was much lower compared to other samples, suggesting a rapid Faradaic process and enhanced kinetics for hydrogen evolution reaction.

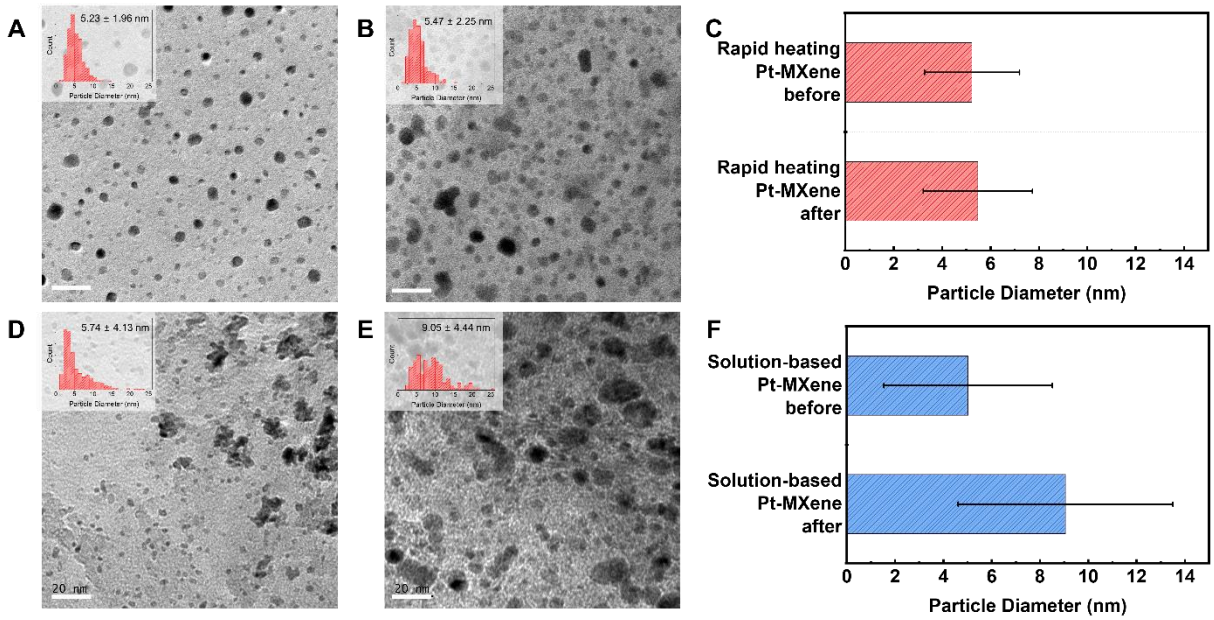

Fig. S19. Pt NPs on MXene surface before and after cycling. TEM images and particle size distribution of Pt NPs of rapid heating Pt-MXene A) before cycling and B) after cycling. C) Organized bar graph showing particle size before and after cycling for rapid heating Pt-MXene. TEM images and particle size distribution of Pt NPs of solution-based Pt-MXene A) before cycling and B) after cycling. C) Organized bar graph showing particle size before and after cycling for solution-based Pt-MXene.

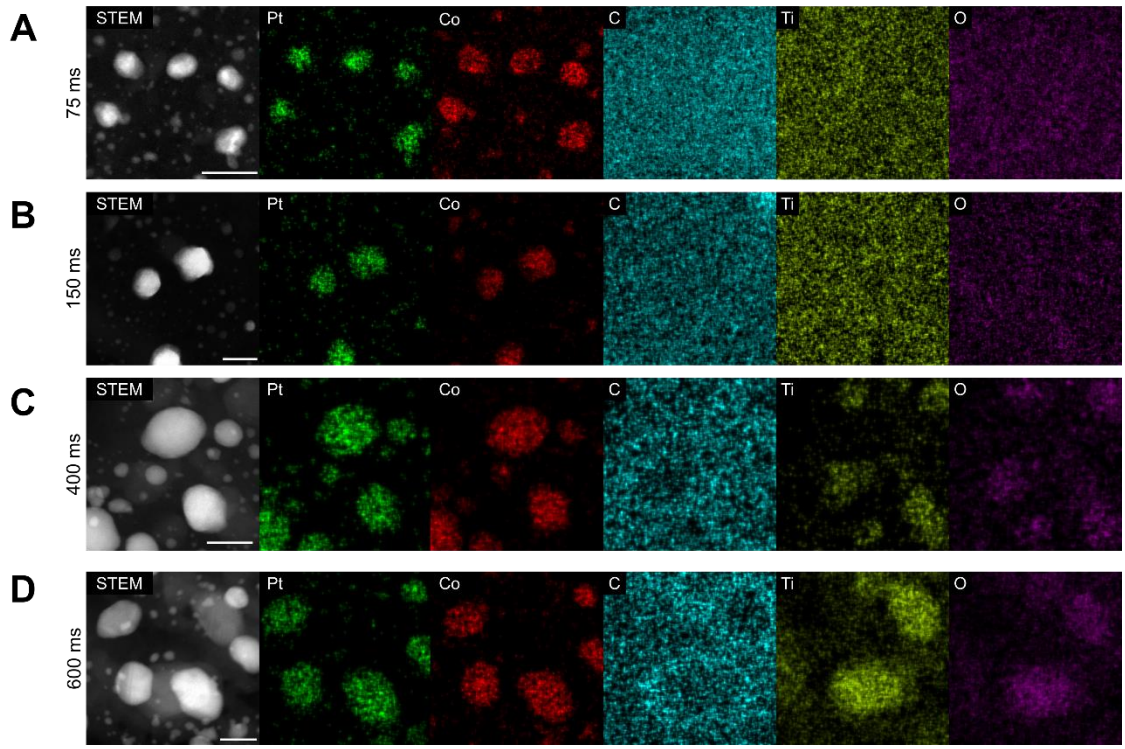

Fig. S20. STEM elemental maps of PtCo bimetallic NPs on MXene surface with varying rapid heating durations. A) 75 ms, B) 150 ms, C) 400 ms, D) 600 ms.

To optimize the polyelemental NP synthesis on MXene surface, different thermal shock durations were tested. The goal is to achieve well-mixed NPs without phase separated states and minimize TiO_2 formation on the surface. When the thermal shock duration was 75 ms, NPs were synthesized but alloy formation was incomplete. One can observe the phase separation in the synthesized NP. With 150 ms of thermal shock, bimetallic NPs were well synthesized without any phase separation. With increase in thermal shock duration, homogeneous alloys were observed but the size of TiO_2 enlarged on the surface

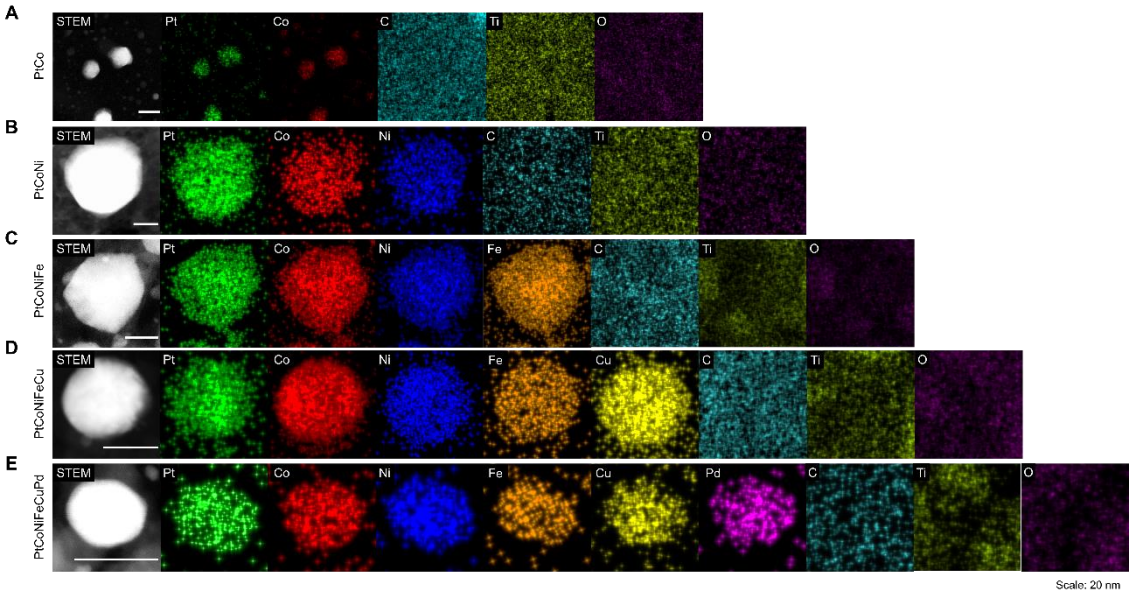

Fig. S21. Various polyelemental NPs on MXene by rapid Joule heating. HADDF-STEM images and comprehensive EDS elemental mapping of various polyelemental NPs on $Ti_3C_2T_x$ MXene for (A) PtCo (B) PtNiCo, (C) PtNiCoFe, (D) PtNiCoFeCu, and (E) PtNiCoCuPd.

Material	Element	Atomic %
Ti_2CT_x	Ti 2p	16.93
	F 1s	12.54
	O 1s	27.70
	C 1s	36.46
	Cl 2p	6.37
$Ti_3C_2T_x$.	Ti 2p	21.67
	F 1s	15.87
	O 1s	18.29
	C 1s	40.88
	Cl 2p	3.3

Table S1. Atomic ratio of different MXenes

Ti_2CT_x and $Ti_3C_2T_x$ MXene differ in its atomic compositions. The high density of surface terminations on Ti_2CT_x, including oxygen and fluoride terminations, may have attributed to the higher density of NPs synthesized on Ti_2CT_x MXene surface.

Catalyst	Overpotential (10 mA cm^{-2})	Tafel slope (mV dec^{-1})	Reference
Mo2TiC2Tx-PtSA	30	30	1
Pt3Ti/Ti3C2Tx-550	32	32	2
Pt@PCM	106	65.3	3
Pt-MoS2	53	40	4
Pt/MXene	34	29.7	5
PtML/Au NF/Ni foam	100	53	6
Pt/def-WO3@CFC	42	61	7
Pt-Ti3C2Tx	67.8	69.8	8
TBA-Ti3C2Tx-Pt-20	55	65	9
Pt SA/WO3-x	47	45	10
Pt-GDY	66	46.6	11
Pt/WS2	80	55	12
Pt-MoS2/NiS2	52	40	13
Pt-Ni3N/Ni@C	45	47.3	14
Pt1@Fe-N-C	60	42	15
MoS2/Ti3C2Tx@C	135	46	16
NiSe2/Ti3C2Tx	200	23.7	17
MoS2/Ti3C2Tx nanoroll	152	70	18
FeNi@Mo2TiC2Tx@NF	165	103.46	19
MoS2-Ti3C2	98	45	20
Ti3C2T@Pt/SWCNTs	62	78	21
Rapid heating Pt-MXene	43.6	40.5	This work

Table S2. HER performance of 2D materials and their heterostructures

References

1. J. Q. Zhang, Y. F. Zhao, X. Guo, C. Chen, C. L. Dong, R. S. Liu, C. P. Han, Y. D. Li, Y. Gogotsi and G. X. Wang, *Nat. Catal.*, 2018, **1**, 985-992.
2. Z. Li, Z. Y. Qi, S. W. Wang, T. Ma, L. Zhou, Z. W. Wu, X. C. Luan, F. Y. Lin, M. D. Chen, J. T. Miller, H. L. Xin, W. Y. Huang and Y. Wu, *Nano Lett.*, 2019, **19**, 5102-5108.
3. H. B. Zhang, P. F. An, W. Zhou, B. Y. Guan, P. Zhang, J. C. Dong and X. W. Lou, *Sci. Adv.*, 2018, **4**, eaao6657.
4. X. Huang, Z. Y. Zeng, S. Y. Bao, M. F. Wang, X. Y. Qi, Z. X. Fan and H. Zhang, *Nat. Commun.*, 2013, **4**, 1444.
5. Y. C. Wu, W. Wei, R. H. Yu, L. X. Xia, X. F. Hong, J. X. Zhu, J. T. Li, L. Lv, W. Chen, Y. Zhao, L. Zhou and L. Q. Mai, *Adv. Funct. Mater.*, 2022, **32**, 2110910.
6. M. Li, Q. Ma, W. Zi, X. J. Liu, X. J. Zhu and S. Z. Liu, *Sci. Adv.*, 2015, **1**, e1400268.
7. H. Tian, X. Z. Cui, L. M. Zeng, L. Su, Y. L. Song and J. L. Shi, *J. Mater. Chem. A*, 2019, **7**, 6285-6293.
8. X. B. Zhang, B. Y. Shao, Z. M. Sun, Z. Gao, Y. Qin, C. Zhang, F. M. Cui and X. J. Yang, *Ind. Eng. Chem. Res.*, 2020, **59**, 1822-1828.

9. Y. Y. Yuan, H. S. Li, L. G. Wang, L. Zhang, D. Shi, Y. X. Hong and J. L. Sun, *ACS Sustain. Chem. Eng.*, 2019, **7**, 4266-4273.
10. J. Park, S. Lee, H. E. Kim, A. Cho, S. Kim, Y. Ye, J. W. Han, H. Lee, J. H. Jang and J. Lee, *Angew. Chem. Int. Ed.*, 2019, **58**, 16038-16042.
11. X. P. Yin, H. J. Wang, S. F. Tang, X. L. Lu, M. Shu, R. Si and T. B. Lu, *Angew. Chem. Int. Ed.*, 2018, **57**, 9382-9386.
12. Y. X. Zhang, J. Q. Yan, X. P. Ren, L. Q. Pang, H. Chen and S. Liu, *Int. J. Hydrog. Energy*, 2017, **42**, 5472-5477.
13. Y. X. Guan, Y. Y. Feng, J. Wan, X. H. Yang, L. Fang, X. Gu, R. R. Liu, Z. Y. Huang, J. Li, J. Luo, C. M. Li and Y. Wang, *Small*, 2018, **14**, 1800697.
14. C. D. Wang, Y. F. Sun, E. L. Tian, D. M. Fu, M. Zhang, X. J. Zhao and W. C. Ye, *Electrochim. Acta*, 2019, **320**, 134597.
15. X. J. Zeng, J. L. Shui, X. F. Liu, Q. T. Liu, Y. C. Li, J. X. Shang, L. R. Zheng and R. H. Yu, *Adv. Energy Mater.*, 2018, **8**, 1701345.
16. X. H. Wu, Z. Y. Wang, M. Z. Yu, L. Y. Xiu and J. S. Qiu, *Adv. Mater.*, 2017, **29**, 1607017.
17. H. M. Jiang, Z. G. Wang, Q. Yang, L. X. Tan, L. C. Dong and M. D. Dong, *Nanomicro Lett.*, 2019, **11**, 31.
18. J. P. Liu, Y. Z. Liu, D. Y. Xu, Y. Z. Zhu, W. C. Peng, Y. Li, F. B. Zhang and X. B. Fan, *Appl. Catal. B: Environ.*, 2019, **241**, 89-94.
19. J. Y. Wang, P. L. He, Y. L. Shen, L. X. Dai, Z. Li, Y. Wu and C. H. An, *Nano Res.*, 2021, **14**, 3474-3481.
20. X. T. Li, X. D. Lv, X. N. Sun, C. Yang, Y. Z. Zheng, L. H. Yang, S. Q. Li and X. Tao, *Appl. Catal. B: Environ.*, 2021, **284**, 119708.
21. C. Cui, R. F. Cheng, H. Zhang, C. Zhang, Y. H. Ma, C. Shi, B. B. Fan, H. L. Wang and X. H. Wang, *Adv. Funct. Mater.*, 2020, **30**, 2000693.